Research Article

The microstructure, degradation behavior and cytotoxicity effect of Mg–Sn–Zn alloys in vitro tests

Ali Ercetin[1] · Özgür Özgün[2] · Kubilay Aslantas[3] · Gürkan Aykutoğlu[4]

Received: 14 October 2019 / Accepted: 6 January 2020 / Published online: 9 January 2020
© Springer Nature Switzerland AG 2020

Abstract
In the present study, Mg5Sn–xZn (x = 0, 1, 2, 3, 4, and 5 wt%) alloys in superior biocorrosion properties were produced successfully. A novel mixing technique which prevents contact of magnesium with oxygen has been applied in order to produce Mg–Sn–Zn alloys by hot pressing. According to the obtained results, it was observed that a homogeneous microstructure could be obtained, and the formed secondary phases were uniformly distributed at the grain boundaries. At the same time, it was determined that addition of Zn had a grain refiner effect on microstructure. Therefore, corrosion resistance increased with increasing Zn ratios. Apatite structures were formed on specimen surfaces during degradation as protective layers. The highest corrosion resistance was obtained from TZ54 alloy, in which the apatite structures formed intensively. The addition of Zn to the alloys had no toxic effects on human neuron cells in terms of biocompatibility, but was effective for cell growth.

Keywords Microstructure · Hot pressing · Degradation behavior · Hydrogen gas measurement · Cytotoxicity

1 Introduction

New biomaterials are continuously being produced in the biomedical field as a result of developing technology. Due to the low mechanical properties of polymer materials, which were one of the first biomaterials, and the lack of sufficient flexibility of ceramic materials, the areas of usage of these biomaterial groups are limited, encouraging research into novel biomaterials [1]. Metallic biomaterials, such as stainless steels and titanium alloys, the strength and fracture toughness of which are superior to those of polymers and ceramics, are used in the cardiovascular, dental, and orthopaedic fields due to their superiority [2].

Metallic biomaterials maintain mechanical integrity during tissue healing [2]; however, some release toxic ions that cause severe allergic reactions, such as local anaphylaxis and inflammation, which can cause life-threatening conditions during degradation [3]. These conventional biometals, which are used as temporary implants, do not degrade in the physiological environment and must be removed by a surgical procedure after healing. The demand for temporary implant materials, such as screws, plates, or stents, is constantly increasing; however, the fact that surgery must be repeated after the improvement is a concern for patients [4]. Material scientists and engineers are therefore investigating novel biodegradable materials that will replace conventional biomaterials [5].

Biodegradable materials melt following completion of the healing process, and therefore no further surgery is required to remove these implants [4, 6]. Such materials must degrade in the body; thus, it is important that the soluble products can be metabolised and biologically

✉ Ali Ercetin, aliercetin@bingol.edu.tr; Özgür Özgün, oozgun@bingol.edu.tr; Kubilay Aslantas, aslantas@aku.edu.tr; Gürkan Aykutoğlu, gaykutoglu@bingol.edu.tr | [1]Department of Mechanical Engineering, Faculty of Engineering and Architecture, Bingol University, 12000 Bingol, Turkey. [2]Department of Occupational Health and Safety, Faculty of Health Sciences, Bingol University, 12000 Bingol, Turkey. [3]Department of Mechanical Engineering, Faculty of Technology, Afyon Kocatepe University, 03200 Afyon, Turkey. [4]Department of Molecular Biology and Genetics, Faculty of Science and Literature, Bingol University, 12000 Bingol, Turkey.

SN Applied Sciences (2020) 2:173 | https://doi.org/10.1007/s42452-020-1988-9

absorbed [6]. Biodegradable implants must have several specific features including adequate stability, moderate and homogeneous degradation, full bone regeneration within 12–15 months, and biocompatibility [7]. Magnesium (Mg) and Mg alloys are among the most obvious choices for biomaterials due to their biocompatibility and superior corrosion resistance [8, 9]. The density of these alloys is in the range of 1.74–2.0 g/cm^3, which is much lower than that of conventional titanium (Ti)-based biomaterials (4.4–4.5 g/cm^3) and relatively similar to bone density (1.8–2.1 g/cm^3) [10]. The elasticity modulus of Mg (41–45 GPa), which is higher than the fracture toughness of ceramic biomaterials, is similar to that of human bone. The daily intake of Mg for a normal human body is 300–400 mg, a necessary element for human metabolism [11]. Mg ions (cofactors) not found in protein structure are essential for the activation of many enzymes and the stabilsation of DNA and RNA structures [12]. It is thought that Mg-based alloys meet some of the requirements of a biomaterial [10]; however, during the early biodegradation phase in the body, when rapid losses in strength are considered, the strength of pure Mg is not high enough [13]. For this reason, novel Mg alloys should be produced via the addition of new alloying elements to Mg in order to improve biocompatibility and corrosion properties.

The alloying elements, Sn and Zn, have attracted attention since they belong to the group of basic elements in the human body. When these elements form a certain ratio of alloy with Mg, they have a significant effect on the microstructure, corrosion resistance and biocompatibility. There have been many studies regarding the production of Mg–Sn alloys by the casting method. A definite conclusion of these studies is that Sn addition up to 5% by weight increases corrosion properties; however, with addition of Sn above this value, toxic effects occur in cells, and the corrosion resistance decreases [14]. The reason for choosing 5% Sn in determining Mg5Sn–xZn alloy composition in the present study is that the addition of a greater ratio results in an increased amount of H_2 gas being released by the galvanic corrosion of the alloy, lowering the corrosion resistance and facilitating faster processing of the corrosion mechanism. In similar studies on the corrosion of Mg–Sn alloys, the chosen Sn ratio has not been above 5% by weight [14, 15]. Furthermore, in cell culture studies, Mg–Sn alloys produced by the addition of Sn above this ratio have been found to damage MG63 cells (bone) [16]. With the addition of the Zn, which is known to play an active role in the growth of human cells, it is possible to produce more advanced Mg alloys [17, 18].

It has been determined from the literature that the production of biomedical Mg alloys is generally carried out by the casting method, and the number of studies using the conventional P/M method is almost negligible due to the high reactivity of Mg with oxygen. However, it is a well-known fact that products with a better microstructure can be obtained by providing homogenous grain distribution in the materials produced by the P/M method [19, 20], and that the corrosion resistance of biomedical materials is directly related to the microstructure [21]. Therefore, the aims of the present study were the application of new methods to enable the production of Mg alloys by the P/M technique, creating biomaterials with superior biocorrosion properties, determining Zn effect on degradation behaviour of Mg–Sn–Zn alloys and investigating the toxic effects of these alloys on human neuron cells (SH-SY5Y).

2 Materials and methods

2.1 Material production

Mg powder (– 45 µm, 99.8%), Sn powder (– 10 µm, 99.9%) and Zn powder (– 10 µm, 99.9%) were used in present study. Sn was added to the Mg powder at a constant rate (5 wt%) and Zn at different rates (0, 1, 2, 3, 4, 5 wt%). The Mg powders were coated with paraffin wax up to 20% of the volume in a vacuum cabin to protect the contact of Mg with air. A Precisa precision scale with 10^{-4} accuracy was used to measure powder weights. Table 1 shows the chemical compositions of the Mg5Sn–xZn alloys. In this system where the pressing and sintering processes were simultaneously applied, the sintering process was carried out in graphite molds at 635 °C under 50 MPa pressure for 30 min in a high purity, protective argon gas atmosphere.

2.2 Microstructure investigation

The alloys were applied to 100, 320, 400, 600, 800, 1000, 1200, and 1500 grit grinding stages for preparation for metallographic examination. Processes of cleaning with absolute ethyl alcohol, drying in desiccator and polishing with 1-µm diamond suspension were carried out according to the literature [15, 22] The alloys were etched with

Table 1 The chemical compositions of the Mg5Sn–xZn alloys

%wt Sn	%wt Zn	%wt Mg	Standard nomenclature
5	0	Balance	TZ50
5	1	Balance	TZ51
5	2	Balance	TZ52
5	3	Balance	TZ53
5	4	Balance	TZ54
5	5	Balance	TZ55

using a mixture of 95% ethyl alcohol and 5% nitric acid (HNO_3), which is well used in Mg-based alloys [23–25]. After etching, the alloys were cleaned with distiled water and absolute ethyl alcohol. For microstructure investigation of the alloys, scanning electron microscope (SEM), energy dispersive spectroscopy (EDS) device and X-ray diffractometer (XRD) analysis were applied.

The success of sintering process was determined by measuring the relative density of specimens. In the calculation of relative density, the literature study was taken into consideration [20]. Theoretical density values were calculated according to rule of mixture. The densities were measured by the Archimedes water displacement method. Relative densities were obtained by the ratio of the measured density value to the theoretical density.

2.3 Corrosion tests

Corrosion tests were carried out according to ASTM-G31-72 standards [26, 27]. The corrosion behaviours of the Mg5Sn–xZn alloys in Hank's solution were determined by considering the amount of released H_2 gas and % weight losses. The chemical composition of Hank's solution is given in Table 2. The surface areas of each alloy were calculated in cm^2 to determine the amount of corrosion liquid to be applied. For the % weight losses and H_2 measurements, the amount of corrosion liquid was adjusted so that the ratio of the amount (mL) of Hank's solution to the surface area (cm^2) of the alloy was 20:1 (mL/cm^2). Each of the Mg5Sn–xZn alloys of different compositions was prepared in $10 \times 10 \times 3$ mm dimensions for corrosion tests. After corrosion testing, the new phases formed on the surface of the specimens were determined by XRD analysis, and the elemental distribution of the microstructure was determined by EDS analysis. Since the conductivity of the specimens is reduced after corrosion testing and it is difficult to obtain images on the SEM/EDS device; gold filament coating was applied to the specimens prior to EDS inspection.

Table 2 The chemical composition of Hank's solution (g/L) [28]

Chemical formula	Quantity (g/L)	Chemical formula	Quantity (g/L)
NaCl	8.00	$MgSO_4 \cdot 7H_2O$	0.20
KCl	0.40	$Na_2HPO_4 \cdot 12H_2O$	0.12
$CaCl_2$	0.14	KH_2PO_4	0.06
$NaHCO_3$	0.35		

2.3.1 Determination of % weight loss

Specimens were subjected to grinding processes between 100 and 1500 grit. After grinding, each specimen was thoroughly cleaned with distilled water and absolute ethyl alcohol and allowed to dry in a desiccator. The weight of each specimen was measured after drying. For each alloy, Hank's solution was predetermined in a 250-mL beaker and the alloys of different composition were placed in separate beakers. Every 24 h, the specimens were taken from the corrosion liquid, rinsed with distilled water, and thoroughly cleaned with absolute ethyl alcohol. The specimens were placed in a desiccator for 1 h to completely remove moisture. After the drying process, the weights of the specimens were measured, the corrosion fluids in each beaker were renewed, and the specimens were returned to the corrosion environment. Measurements continued until 240 h. Equation 1 was used to determine the weight loss of each alloy [14]. Degradation rates (mm/year) of the specimens were obtained using Eq. 2 [29]. The terms specified in Eq. 2; constant coefficient $K = 8.76 \times 10^4$, specimen weight loss W (g), specimen total surface area A (cm^2), corrosion exposure time T (h), and specimen density D (g/cm^3) are defined as [29].

$$\text{Total weight loss}\,(\%) = \frac{(\textit{First weight} - \textit{last weight})\,\textit{of specimen}}{\textit{First weight of specimen}} \times 100 \tag{1}$$

$$\text{Corrosion rate}\,(\text{mm/year}) = \frac{(K * W)}{(A * T * D)} \tag{2}$$

2.3.2 Hydrogen gas measurements

The hydrogen gas released during the degradation of the alloys in Hank's solution was measured as described in the literature [22, 30, 31]. A 250-mL beaker was used for each alloy and a 50-mL graduated cylinder with 0.01 mL sensitivity was used in the system. The Hank's solution, the volume of which was determined by the surface area of the specimens, was measured using a graduated cylinder and the specimens were dropped herein. The 250-mL beaker and cylinder were inverted 180°. Therefore, the specimens were located at the mouth of the graduated cylinder and at the bottom of the beaker. The specimens were positioned in this way in a specifically manufactured heating cabinet at a constant physiological temperature of 37 °C. The heating system operated

at a precision of 0.1 °C and controlled the temperature in two different zones of the heating cabinet. The corrosion fluid was renewed every 24 h. Over time, H_2 gas began to accumulate at the top of the scale. To determine the amount of H_2 gas deposited in the graduated cylinder, the amount of liquid in the graduated cylinder was measured when the specimens were left in the heating cabinet and every 24 h for a total of 240 h.

2.4 Cell culture tests

Cells were maintained in 500 mL RPMI 1640 medium supplemented with 10 mL fetal bovine serum per 89 mL medium plus 1 mL penicillin-streptomycin. Powders of Mg5Sn–xZn alloys of 6 different compositions were added to 50-mL tubes containing medium and allowed to dissolve for a few weeks.

Human neuron cells (SH-SY5Y) were obtained from the Central Laboratory of Bingöl University in cryotubes stored at − 80 °C. The cells were transferred to 15-mL tubes containing medium and centrifuged at 2500 rpm for 3 min to pellet the cells. The medium was removed and replaced with 4 mL fresh medium, which was then transferred to a T-25 cell culture flask. The cells were placed in an incubator at 5% CO_2, 37 °C and allowed to adhere, followed by the daily removal of dead floating cells and renewal of the medium.

When the cells reached 80% confluence, they were detached from the flask using 1 mL trypsin, and medium containing serum was added to inactivate the trypsin. The cells were centrifuged for 2 min at 2500 rpm for pelleting and resuspended in fresh medium. The cells were subsequently seeded in a 96-well plate at a volume of 100 µL (at least 10,000 cells) and placed at 37 °C, 5% CO_2 for 24 h.

In each well of the first row, 100 µL media was aspirated, leaving the cells on the bottom of each well. Mg5Sn–xZn alloys were dissolved in RPMI 1640 medium at a constant concentration (250 µg/mL) to determine the toxicity effect of these alloys on human neuron cells (SH-SY5Y). Previously prepared Mg5Sn–xZn alloy solutions in medium were added to each well at a volume of 200 µL (3 columns per alloy composition). Beginning from the first column, the solution was mixed into second row by taking 100 µL from first row; accordingly, the dose of the alloy solution was halved in each row. Fluid transfer ended at seventh row. Last row was left as the control without fluid transfer. The same procedure was applied to the other columns. The 96-well plates were returned to the incubator and the alloy solutions were allowed to act on the cells for 24 h. A volume of 3 µL WST-1 was added to each well to determine the degree of effect of the alloy solutions on the cells. After a 3-hour incubation, the absorbance of each well was measured at 450 nm using an ELISA plate reader and the viability of SH-SY5Y cells was assessed. Statistical analysis of the data was performed using the Graphpad Prism 5 software. The statistical comparison of the groups was carried out using Dunnett's test, and statistical significance was analysed using one-way ANOVA. A significance level was set at $p < 0.05$. The measurements in each group were performed in at least triplicate.

3 Results and discussion

3.1 Evaluation of density and relative density data of the alloys

Figure 1 shows the density and relative density values of Mg5Sn–xZn alloys produced by the hot pressing. Density values of the alloys always increased with increasing Zn ratios which were very close to the theoretical density values. It can be understood from Fig. 1 that relative density values of all alloys were over 99% and sintering process were succesfull. In a similar study by Turan et al. [32], it was reported that successful sintering process was carried out with obtaining relative density values over 99%.

3.2 XRD results before and after immersion

The phase compositions of the Mg5Sn–xZn alloys were examined by XRD analysis (Fig. 2a). Hot pressed-sintered all alloys had typical α-Mg and Mg_2Sn phase. TZ55 alloy also contains one more phase (MgZn phase). No peaks of the MgO phase were found, indicating that oxidation can be prevented throughout the entire production process, from paraffin coating of the Mg powders, to mixing with other powders and the P/M sintering of alloys. The peak intensity of Mg_2Sn phase was the same in all patterns. Hovewer, the peak intensity of α-Mg phase decreased with increasing Zn content, which indicated a formation

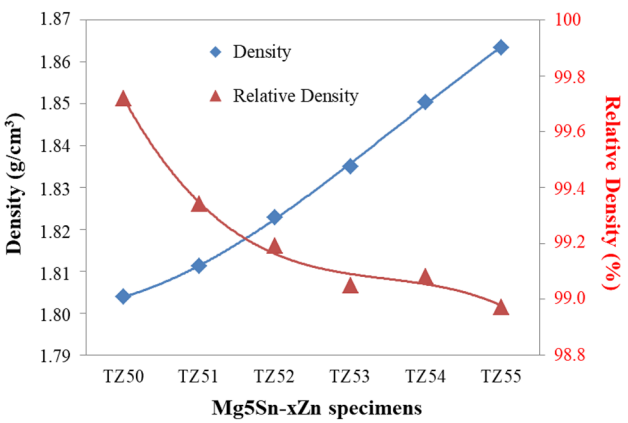

Fig. 1 Density and relative density values of alloys

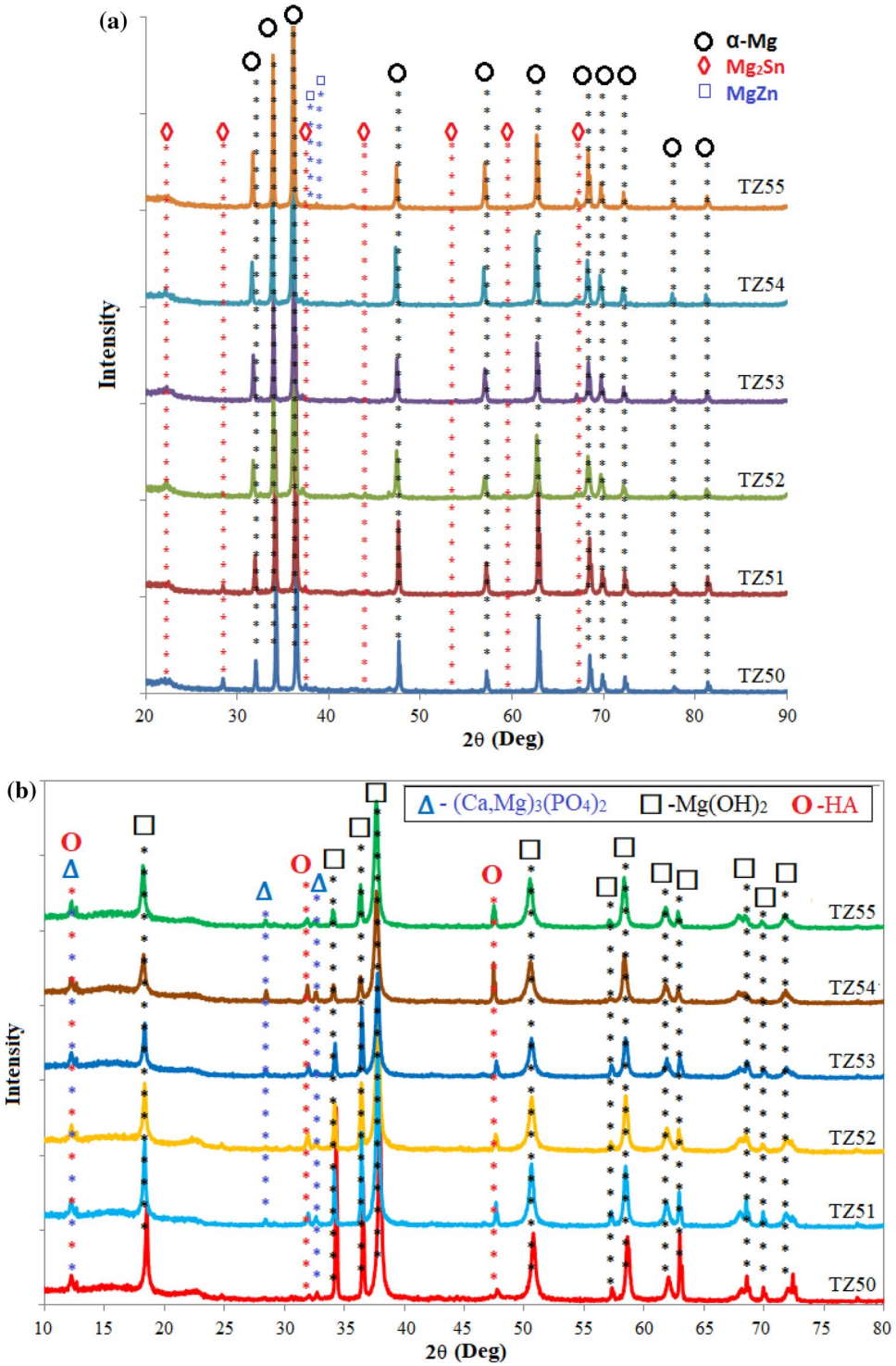

Fig. 2 XRD patterns of alloy specimens; **a** before immersion, **b** after immersion in Hank's solution for 240 h

of MgZn phase. Existence of these phases were supported by XRD analyses in similar literature studies [18, 33]. In present study, MgZn phase was not observed in patterns of Mg5Sn–xZn alloys containing less than 5% by weight of Zn. In a similar study Ha et al. [34], the MgZn phase was not found by XRD analyses containing up to 5% by weight of Zn. In another studies on Mg–Zn alloys [17, 35, 36], it has been determined that the presence of peaks of the MgZn phase are present in the XRD patterns of materials containing greater than 5% Zn.

The XRD patterns after immersion of Mg5Sn–xZn alloys in Hank's solution for 240 h are given in Fig. 2b, indicating

that corrosive products contain a calcium phosphate-based ceramic hydroxyapatite (HA), magnesium hydroxide ($Mg(OH)_2$), and a kind of magnesium-doped apatite $(Ca, Mg)_3(PO_4)_2$. According to a study by Kuwahara et al. [37], magnesium-doped apatite was found in corrosion residues after immersion in Hank's solution. It was mentioned that this type of amorphous magnesium-doped apatite may occur during the corrosion process in the corrosion layer. In a similar study by Zhang et al. [38], HA and $Mg(OH)_2$ peaks were obtained when XRD analysis was applied to Mg–Zn alloy after immersion. In the present study, it was observed that the $Mg(OH)_2$ peaks decreased and the HA peaks increased in the specimens as determined by XRD analysis; however, the formation of new $(Ca, Mg)_3(PO_4)_2$ peak intensities in the regions where the $Mg(OH)_2$ peaks are decreased can also be observed in Fig. 2b. It is thought that the $Mg(OH)_2$ structures in the passive film layer are dissolved in Hank's solution and combined with phosphate structures to form the new apatite peaks. The formation of apatite structures is described in detail in the analysis of H_2 gas formation during corrosion.

3.3 SEM/EDS analysis before and after immersion

SEM and EDS analysis were used to investigate the microstructure of Mg5Sn–xZn alloys before and after immersion. SEM and EDS images of specimen surfaces before immersion were given in Figs. 3a and 4a. When SEM images are examined, it is seen that the alloys have a nonporous microstructure. Obtaining the relative density values in Fig. 1 above about 99% supports these nonporous SEM images. Bright particles in microstructure were uniformly distributed throughout the grain boundaries. From the EDS analysis in the present study (Fig. 4a), gray areas were

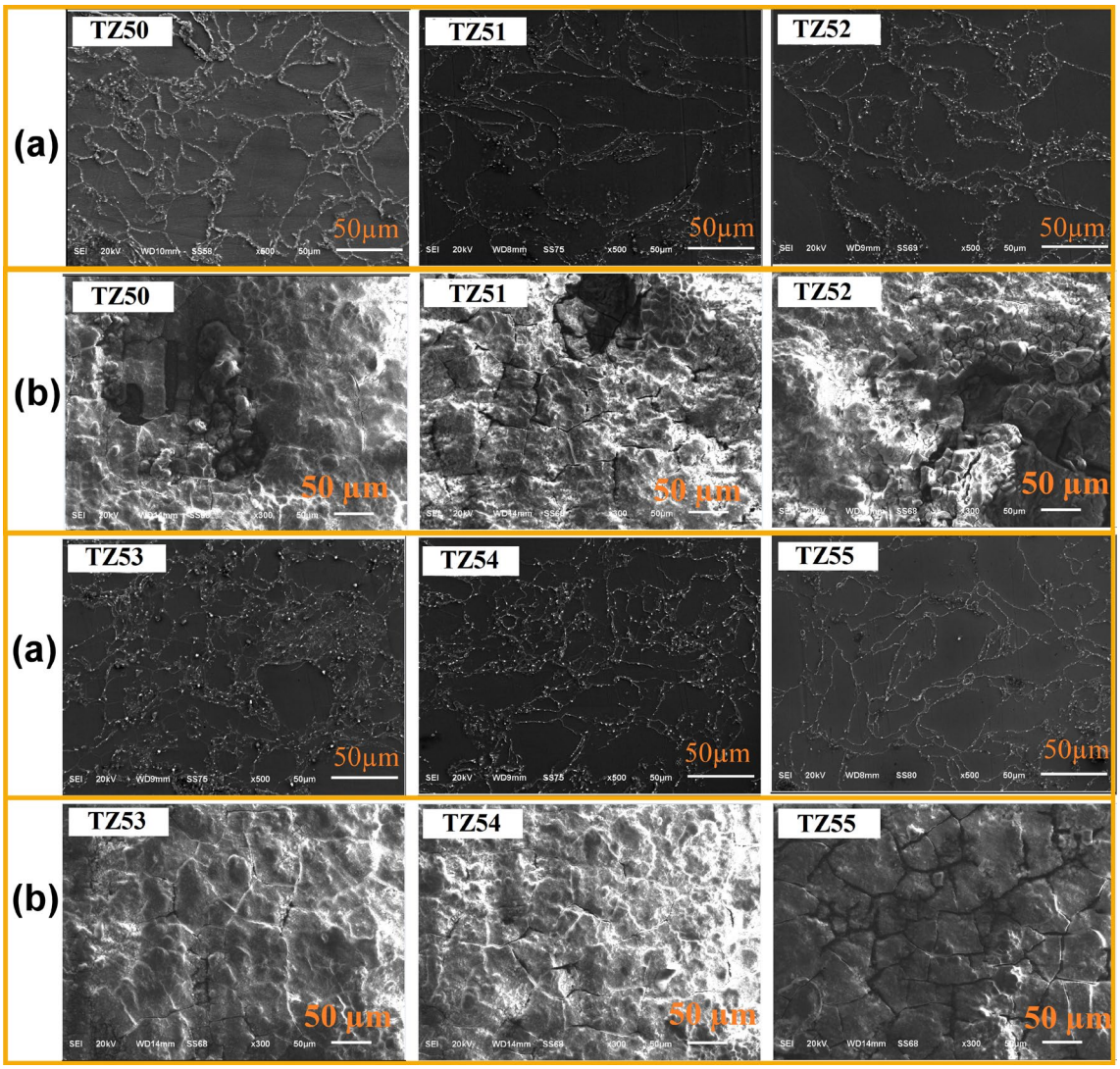

Fig. 3 SEM images of surface morphology of Mg5Sn–xZn alloys; **a** before immersion, **b** after immersion in Hank's solution for 10 days

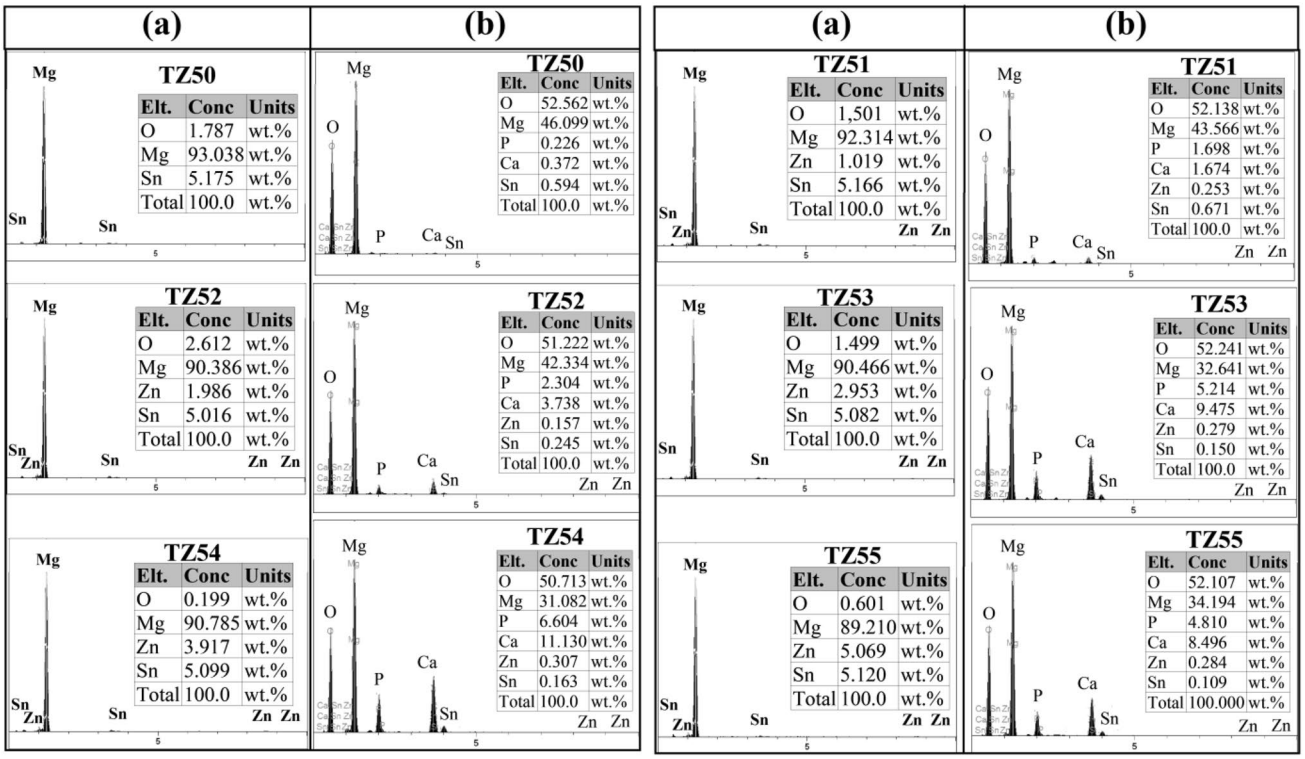

Fig. 4 Areal EDS analysis from surface of Mg5Sn–xZn alloy specimens; **a** before immersion, **b** after immersion in Hank's solution for 10 days

rich in Mg and bright areas were rich in Sn. Zn content becomes richer in bright areas with increasing Zn ratio of Mg5Sn–xZn alloys. The elemental EDS analysis results are very close to the composition values determined for Sn and Zn alloying elements. As determined by XRD analysis (Fig. 2a), gray areas were α-Mg phase and bright areas were Mg_2Sn phase and also MgZn phase with increasing Zn content. In the present study, all Sn and Zn were melted during the hot press process at 635 °C when Mg powders were still solid. According to phase diagrams [39], Sn and Zn were soluble in Mg at 635 °C. Solubility in Mg at room temperature is 2 wt% for Zn and 0 wt% for Sn. However, the specimens were cooled very fast to room temperature after sintering and the Sn atoms were completely precipitated from the Mg during this decrease in temperature, forming a new phase (Mg_2Sn), while only the Zn atoms greater than 2 wt% were precipitated from the Mg, forming a new phase (MgZn). The SEM images show that Mg_2Sn precipitates (bright particles) were formed at the grain boundaries in particular; this is due to the fact that diffusion is easier at this position. In a similar study [23], it has been reported that rapidly decreasing soluble Sn atoms form Mg_2Sn precipitates due to the reduced temperature during solidification of Mg–Sn alloys produced by casting.

The surface morphologies of the Mg5Sn–xZn alloys of 6 different compositions following immersion in Hank's solution 10 days are given in Fig. 3b. The corrosive products can be seen as a white colour in the SEM images, and cracks are detected on the corrosion surfaces. It is thought that cracks formed on the specimen surfaces due to the H_2 gas evaluation, and the literature supports these ideas [37, 38]. In the TZ50 alloy, which does not contain Zn, more galvanic corrosion occurred. With an increasing amount of Zn, the pits in the corrosion surface were decreased and the morphology improved.

EDS images of the surface morphologies of Mg5Sn–xZn alloys after 10 days of immersion in Hank's solution are given in Fig. 4b. It is clear that there is a corrosion layer containing Mg, O, Ca, and P on the specimen surface, and it is thought that these layers are formed by HA, $Mg(OH)_2$, and $(Ca,Mg)_3(PO_4)_2$, the peaks of which were determined through XRD analysis. EDS analysis (Fig. 4b) of the TZ50 alloy specimen without Zn shows that the surface layer is composed of Mg and O. H element could not be detected in the elemental analysis, since the atomic radius of H is too small to be detected; however, this structure is thought to contain intense $Mg(OH)_2$. There are very small amounts of Ca and P elements on the surface structure of the same specimen, showing the existence of a small amount of HA. The higher Ca and P ratios in the specimens containing Zn indicate that the apatite structures containing Ca and phosphate (PO_4^{-3}) are higher in these specimens. The

percentages of P and Ca seen in the EDS results prove this (Fig. 4b). In a similar study by Zhang et al. [38], the Ca and P ratios obtained by EDS analysis from the HA structure after the corrosion process applied to Mg6Zn alloys are very similar to those obtained from Zn-containing specimens in the present study. Another result that can be derived from the EDS analysis of the specimens in the present study is that the formation of apatite structures increased on the surface, as can be seen from the elemental distributions obtained from the corrosion surfaces, which are protective structures due to increasing Zn in the specimens. It can be seen that these structures are concentrated in grain boundaries, and it is thought that apatite structures serve as a barrier and increase corrosion resistance. More detailed information is given in the section on the assessment of H_2 gas measurement during degradation.

3.4 Evaluation of weight loss measurements

Figure 5b shows the percentage weight loss measurements of Mg5Sn–xZn alloys in Hank's solution every 24 h. The greater the weight loss of a material in corrosion liquid, the lower the corrosion resistance of the material and the higher the corrosion rate; thus, the specimen with the least weight loss would have the highest corrosion resistance. From Fig. 5b, it can be seen that the corrosion rate decreases with time; this is because magnesium hydroxide and other apatite structures that form on the corrosion surface have protective and anti-degradation properties. In the literature [38], it is stated that corrosive products behave as a protective layer. Another point that is noteworthy in the graph is that as the amount of Zn added to the Mg5Sn–xZn alloys reaches 4% by weight, the minimum weight loss occurs in the specimen and the highest corrosion resistance in Hank's solution is obtained in the TZ54 alloy. In the microstructure analysis section of the present study, it was mentioned that the intermetallic phases are homogeneously distributed in the grain boundaries and finer-grained structures are formed by the addition of Zn, which are thought to have a corrosion-enhancing effect. In a similar study, there was evidence that the formation of a finer grain in the microstructure increases the corrosion

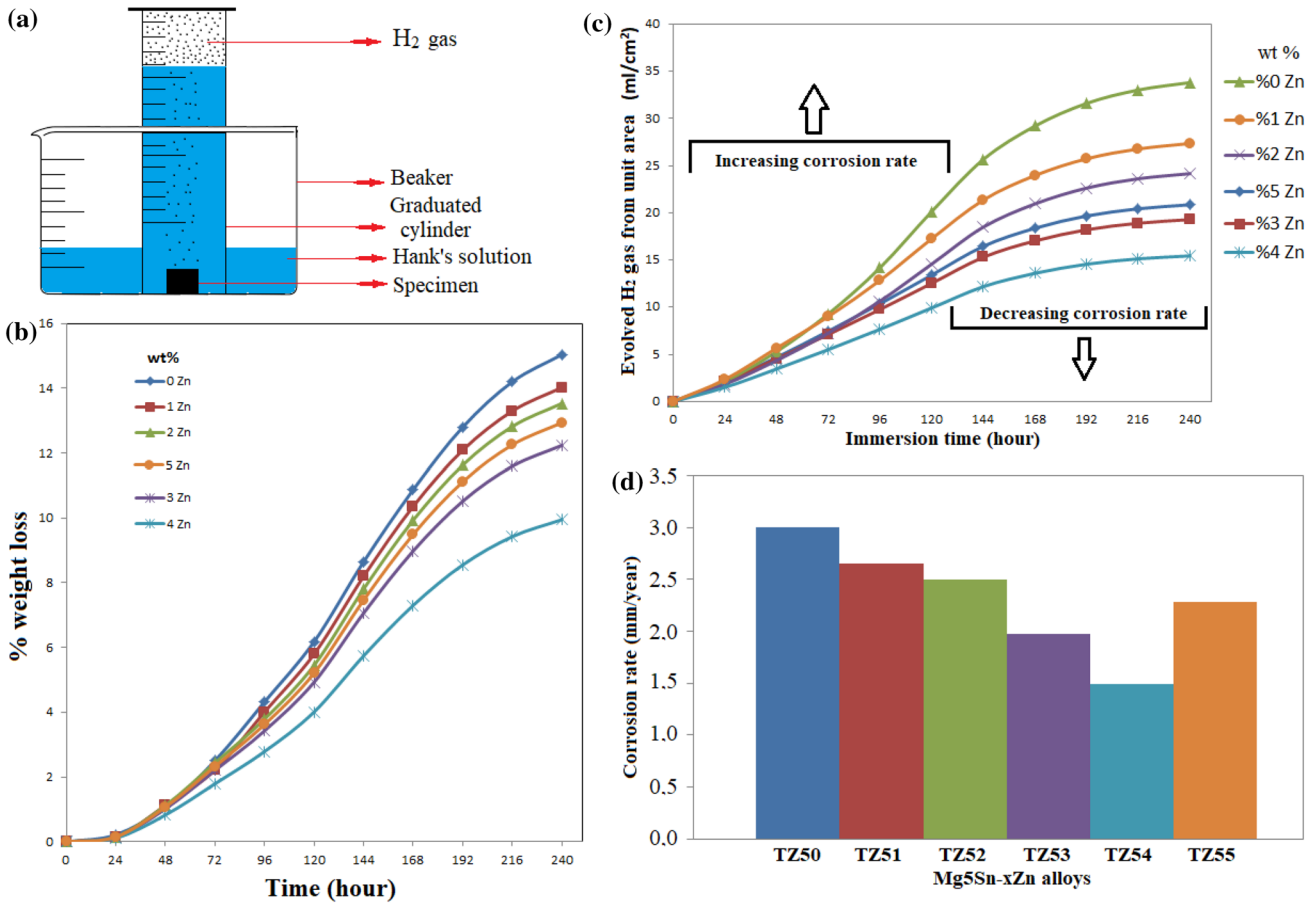

Fig. 5 **a** Measurement method of evolved hydrogen gas, **b** percentage weight loss measurements, **c** graph of H_2 gas evaluation from the unit area, **d** corrosion rates of Mg5Sn–xZn alloys in Hank's solution

resistance [15]. According to another study [40], microstructural parameters, such as phase distribution and grain size, affect the degradation behaviour of Mg-based alloys. As the alloy microstructure changes according to the production method, the corrosion properties of Mg alloys also change. Owing to the rapid solidification, a homogenous and fine-grained microstructure can be formed, which increases the corrosion resistance of the alloys [40].

With an increase in Zn addition, the percentage weight loss rate decreased overall; however, although the TZ55 alloy contains the highest proportion of Zn (5% by weight) as compared with the other alloys, the corrosion resistance of this alloy is shown to be reduced (Fig. 5b). It is thought that the MgZn intermetallic phase caused this situation as determined by XRD analysis shown in Fig. 3 and was formed only in the TZ55 alloy. In the literature [41], galvanic corrosion generally begins with a defect in the vicinity of the intermetallic phases under passive film. The behaviours of the Mg matrix, as an anode, and the cathode caused intermetallic secondary phase particles to be observed at the grain boundaries, accelerating the degradation events in these regions [17, 41]. For example, during corrosion tests in the 3.5% NaCl solution of the AM60 alloy, galvanic corrosion began in the vicinity of the Al–Mn particles [41]. Cai et al. [17], investigated the corrosion properties of the alloys obtained by adding Zn to 3%, 5%, and 7% by weight. According to their results, MgZn phases were determined in alloys containing 5% and 7% Zn, and the corrosion resistance of these alloys decreased due to an increase in Zn ratio. The decrease in corrosion resistance was attributed to two reasons. Firstly, the intensity of MgZn peaks obtained by XRD analysis increased with increasing amounts of Zn. The increased amount of secondary phase produced more anodic and cathodic boundaries, thus causing more galvanic corrosion at these limits. Secondly, in these alloys produced by the casting method, the secondary phases distributed in the grain boundaries are in the form of a continuous web, increasing the anodic and cathodic boundaries and causing more galvanic corrosion to occur. In the present study, the SEM images of the Mg5Sn–xZn alloys produced by the hot pressing using the P/M technique (Fig. 4) show that the secondary phases are not continuous webs in the grain boundaries but instead occur in discontinuous form. Therefore, the corrosion resistance properties obtained in the present study are better than those reported in the literature [14, 15, 17, 34]. In another similar study regarding the effect of secondary phases on corrosion resistance [14], corrosion rates were applied to Mg–Sn alloys containing different amounts of Sn. It is known that there is an increase in the Mg_2Sn phase with an increase in the amount of Sn, which leads to more galvanic corrosion and a decrease in corrosion resistance.

In the present study, the TZ54 alloy produced by the hot pressing had a weight of 365.9 mg prior to immersion in Hank's solution, and after 10 days of immersion, its weight decreased to 329.4 mg. The corrosion rate of this alloy was determined as 3.65 mg/day, which is much lower than the corrosion rate of the coated AZ31 alloy (8 mg/day), which is currently used as a biomedical material [42].

3.5 Evaluation of evolved hydrogen gas and corrosion rate

The graph of H_2 gas evaluation from the unit area of Mg5Sn–xZn alloys during immersion in Hank's solution is shown in Fig. 5c. During the immersion time in Hank's solution for 120 h, there was an increase in the amount of evolved H_2 gas. After 120 h of immersion, reductions in the evolved H_2 gas volume measured at intervals of 24 h continued until 240 h. Thus, the corrosion rate increased continuously for the first 120 h (5 days) but slowed down during the last 120 h (last 5 days). At the beginning of the immersion process, the specimen surface is protected due to the oxide/hydroxide film; however, this film begins to dissolve in basic medium or by degradation by Cl^- ions. The surface area of the specimen is increased as the surface dissolves; therefore, the H_2 gas outlet rate also increases. As a result of diffusion control after a certain time, the H_2 gas outlet rate remains constant. It is also possible to explain the relationship between the volume of evolved H_2 gas and the corrosion rate by referring to the corrosion mechanism. Magnesium is dissolved in Hank's solution according to the reactions in Eqs. 3, 4, 5 and 6 [14, 15].

$$Mg \rightarrow Mg^{2+} + 2e^{-}(\text{anodic reaction}) \quad (3)$$

$$2H_2O + 2e^{-} \rightarrow 2OH^{-} + H_2(\text{cathodic reaction}) \quad (4)$$

$$Mg^{2+} + 2OH^{-} \rightarrow Mg(OH)_2(\text{product formation}) \quad (5)$$

$$Mg + 2H_2O \rightarrow Mg(OH)_2 + H_2(\text{total reaction}) \quad (6)$$

As understood from Eqs. 3, 4, 5 and 6, the more $Mg(OH)_2$ forms as the corrosive product, the more H_2 gas is released. The graph of XRD analysis of the specimens after immersion (Fig. 2b) shows that the highest peak intensity values for the $Mg(OH)_2$ phase were obtained from the TZ50 alloy without Zn. As expected, according to the graph in Fig. 5c, the maximum amount of evolved H_2 gas was obtained from this alloy. Passive $Mg(OH)_2$ film structures also increase with increased corrosion. During the decrease in corrosion rate, it is thought that this passive

film is transformed into apatite structures with phosphate content, and the corrosion rate decreases due to the fact that these apatite structures are more stable. This situation has been explained in the literature as follows [38, 42].

The free Cl^- ions in Hank's solution convert the structure of $Mg(OH)_2$ into $MgCl_2$ as in Eq. 7 [43]. The $MgCl_2$ structure is dissolved in Mg^{2+} and $2Cl^-$ ions and settles on the surface of the specimen, leaving the OH^- in the environment [44]. As a result, free phosphate ions ($H_2PO_4^-$, HPO_4^{-2}, and PO_4^{-3}) (Eq. 8) and Ca^{2+} ions in Hank's solution can react with OH^- to form HA and other apatite structures as determined by XRD analysis according to Eq. 9 [45]. Therefore, Mg^{2+} ions in biological apatites are one of the main substitutes, and it is possible that the magnesium-doped apatite structure is precipitated on the specimen surface [37]. As a result, corrosive products containing HA and other magnesium-doped apatites can reduce the corrosion rate by forming a protective layer on the surface via the filling of corrosion cracks [38].

$$Mg(OH)_2 + 2Cl^- \rightarrow MgCl_2 + 2OH^- \quad (7)$$

$$H_2PO_4^- \rightarrow HPO_4^{-2} + PO_4^{-3} \quad (8)$$

$$10Ca^{+2} + 6PO_4^{-3} + 2OH^- \rightarrow Ca_{10}(PO_4)_6(OH)_2 \quad (9)$$

The reasons for the differences in corrosion rates between the start and end of corrosion tests are now understood. In the present study, as can be seen from the XRD analysis in Fig. 2b and the EDS analysis in Fig. 4b, Mg5Sn–xZn specimens with a greater amount of apatite structures in the surface morphology were exposed to less corrosion. It was determined that the apatite structures formed a protective layer on the surface, which decreased the corrosion rates (Fig. 5d) of the specimens. For this reason, most apatite structures were formed on the surface of the TZ54 alloy. Accordingly, in the present study, the lowest H_2 gas content was obtained from the TZ54 alloy, with a value of approximately 15 mL/cm^2. In a similar study, Shuai et al. [15], applied immersion in Hank's solution to determine the corrosion properties of Zn-containing MgSnZn alloys produced by the conventional P/M method and measured the volume of evolved H_2 gas from the surface of the alloys during corrosion. The lowest H_2 gas measurement of approximately 40 mL/cm^2 was obtained from the Mg5Sn4Zn alloy. In the literature [46], it is mentioned that 1 mg Mg must be dissolved to release 1 mL H_2 gas [11]. It is also known that the daily intake of Mg for a normal adult is between 300 and 400 mg [11]. In the present study, the TZ54 alloy, in which the corrosion rate and volume of evolved H_2 gas were lowest, lost approximately 10% of the amount of Mg that should be taken daily.

Bar graphs of the corrosion rates of Mg5Sn–xZn alloys are given in Fig. 5d. The corrosion rate is generally reduced with increasing Zn content. The lowest corrosion rate is observed following immersion of the TZ54 alloy. With an increase in Zn content from 4 to 5 wt%, the corrosion rate increased. As previously mentioned, this is thought to be due to the MgZn phase, which could only be found in the XRD spectra of the TZ55 alloy. Yim et al. [47], applied an extra heat treatment to homogenise the microstructure of Zn-containing Mg5Sn–xZn alloys produced by the casting method and then subjected them to corrosion tests. Corrosion rates of Zn containing alloys at 1 wt%, 2 wt%, and 3 wt% were approximately 2.6, 2.8, and 3.7 mm/year, respectively. As shown in Fig. 5d, the best corrosion properties obtained in the present study with the TZ54 alloy were 1.49 mm/year, which was 42.6% less than that obtained by Yim et al. [47].

3.6 Cell viability analysis

The graph showing the 24-hour effect of Mg5Sn–xZn alloys on the viability of human neuron cells is given in Fig. 6. These alloys containing different ratios of Zn were dissolved in the medium to concentrations of 3, 7, 15, 31, 62, 125, and 250 µg/mL. There was no effect on SH-SY5Y cell viability at any dose over a 24-hour period; however, cell viability increases due to increasing doses. It is known that Zn plays an important role in the growth of human cells [48]. Gu et al. [48], investigated the effects of binary Mg alloys produced by the casting method on fibroblasts (L-929 and NIH3T3), osteoblasts (MC3T3-E1), and blood vessel-related cells (ECV304 and VSMC). According to their results, increasing Zn concentrations showed increased viability in all cells. Increasing Sn concentrations were also found to have no toxic effects on L-929, NIH3T3, or MC3T3-E1 cells [48].

4 Conclusions

The Mg5Sn–xZn alloys were prepared succesfully by hot press sintering method. The XRD results show that the Mg_2Sn phase was observed in all Mg5Sn–xZn alloys. Hovewer, MgZn phase was formed only in the TZ55 alloy. The added Zn alloying elements provided a finer particle microstructure, thus improving the corrosion properties of the Mg5Sn–xZn alloys. As a result of immersion, the weight loss percentage and amount of evolved hydrogen gas decreased until 4 wt% Zn-containing specimens

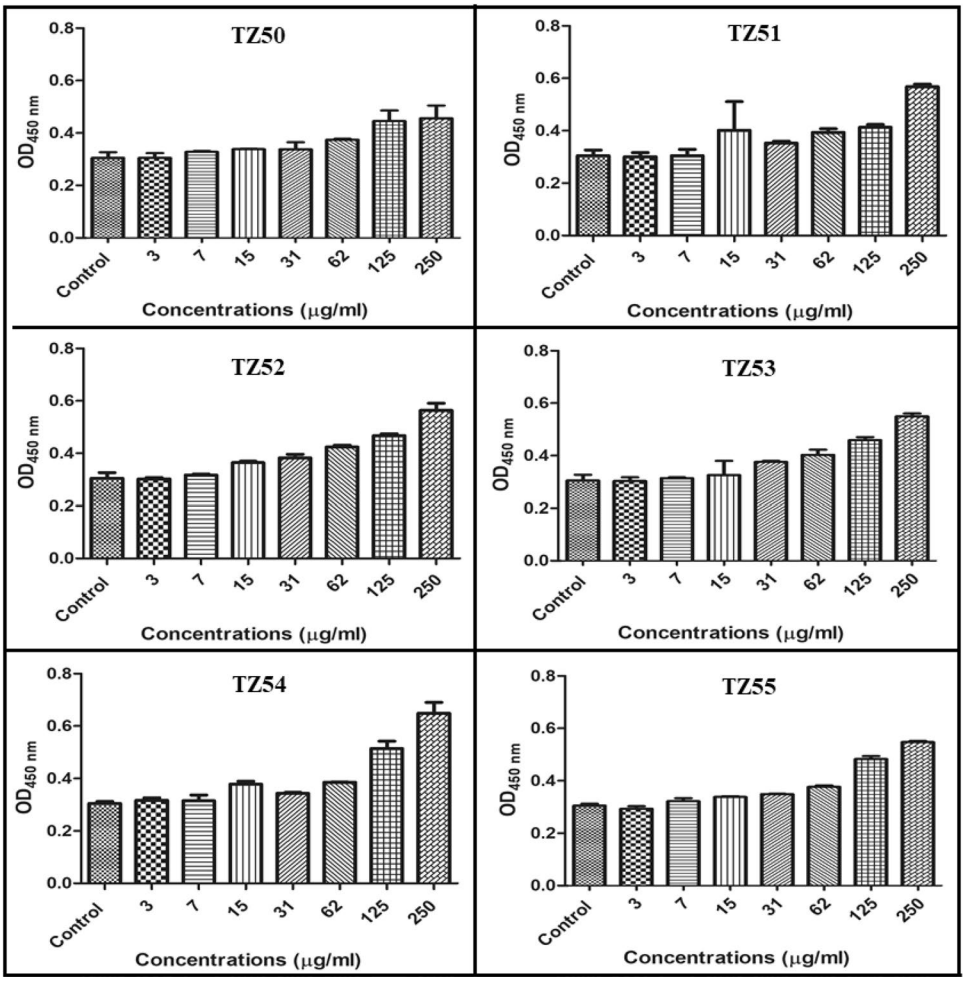

Fig. 6 Effects of Mg5Sn–xZn alloy specimens on SH-SY5Y cells

and increased again in specimens containing 5 wt% Zn because of MgZn phase, so TZ54 alloy showed the best corrosion properties. Hydroxyapatite and magnesium-doped apatite structures were also determined as protective layers on specimen surfaces, which were determined by XRD and EDS analyses. These structures were most commonly observed in the TZ54 alloy, in which the corrosion rate was the lowest. Apatite layers act as a protective layer during degradation. In addition to all these, it was determined that Mg5Sn–xZn alloys did not have a toxic effect on human neuron cells, but were effective for cell growth.

Acknowledgements This work was supported by the Afyon Kocatepe University Scientific Research Projects Coordination Unit of Turkey [18.FEN.BİL.61]. The authors also would like to thank Bingol University Central Research Laboratory of Turkey.

Compliance with ethical standards

Conflict of interest The authors declare no competing financial interests.

References

1. Levesque J, Dube D, Fiset M, Mantovani D (2004) Materials and properties for coronary stents. Adv Mater Process 162:45–48
2. Hu RG, Zhang S, Bu JF, Lin CJ, Song GL (2012) Recent progress in corrosion protection of magnesium alloys by organic coatings. Prog Org Coat 73:129–141
3. Shadanbaz S, Dias GJ (2012) Calcium phosphate coatings on magnesium alloys for biomedical applications: a review. Acta Biomater 8:20–30
4. Park GE, Webster TJ (2005) A review of nanotechnology for the development of beter orthopedic implants. J Biomed Nanotechnol 1:18–29
5. Jung JY, Kwon SJ, Han HS, Lee J-Y, Ahn J-P, Yang S-J, Cho S-Y, Cha P-R, Kim Y-C, Seok H-K (2012) In vivo corrosion mechanism by elemental interdiffusion of biodegradable Mg–Ca alloy. J Biomed Mater Res B 100:2251–2260
6. Hamid H, Coltart J (2007) Miracle stents'-a future without restenosis. McGill J Med 10:105–111
7. Kraus T, Fischerauer SF, Hanzi AC, Uggowitzer PJ, Loffler JF, Weinberg AM (2012) Magnesium alloys for temporary implants in osteo synthesis: in vivo studies of their degradation and interaction with bone. Acta Biomater 8:1230–1238

8. Zhao J, Guo L, Fu YP, Zhao YG, Tan LL, Yang K (2013) In vivo degradation and biocompatibility of magnesium alloy coated with tricalcium phosphate. Rare Metal Mater Eng 42:1013–1016
9. Li HF, Zheng YF, Qin L (2014) Progress of biodegradable metals. Prog Nat Sci Mater Int 24:414–422
10. Li X, Liu X, Wu S, Yeung KWK, Zheng Y, Chu PK (2016) Design of magnesium alloys with controllable degradation for biomedical implants: from bulk to surface. Acta Biomater 45:2–30
11. Song GL, Song SZ (2007) A possible biodegradable magnesium implant material. Adv Eng Mater 9:298–302
12. Staiger MP, Pietak AM, Huadmai J, Dias G (2006) Magnesium and its alloys as orthopedic biomaterials: a review. Biomaterials 27:1728–1734
13. Gu X-N, Zheng Y-F (2010) A review on magnesium alloys as biodegradable materials. Front Mater Sci China 4:111–115
14. Zhou Y-Z, Wu P, Yang Y, Gao D, Feng P, Gao C, Wu H, Liu Y, Bian H, Shuai C (2016) The microstructure, mechanical properties and degradation behavior of laser-melted MgSn alloys. J Alloy Compd 687:109–114
15. Shuai C, Zhou Y, Lin X, Yang Y, Gao C, Shuai X, Wu H, Liu X, Wu P, Feng P (2017) Preparation and characterization of laser-melted Mg–Sn–Zn alloys for biomedical application. J Mater Sci Mater Med 28:1–8
16. Zhao C, Pan F, Zhao S, Pan H, Song K, Tang A (2015) Microstructure, corrosion behavior and cytotoxicity of biodegradable Mg–Sn implant alloys prepared by sub-rapid solidification. Mater Sci Eng C 54:245–251
17. Cai S, Lei T, Li N, Feng F (2012) Effects of Zn on microstructure, mechanical properties and corrosion behavior of Mg–Zn alloys. Mater Sci Eng C 32:2570–2577
18. Qi F, Zhang D, Zhang X, Xu X (2014) Effect of Sn addition on the microstructure and mechanical properties of Mg–6Zn–1Mn (wt%) alloy. J Alloy Compd 585:656–666
19. Gökçe A, Fındık F, Kurt AO (2011) Microstructural examination and properties of premixed Al–Cu–Mg powder metallurgy alloy. Mater Charact 62:730–735
20. Özgün Ö, Aslantaş K, Erçetin A (2019) Powder metallurgy Mg–Sn alloys: production and characterization. Sci Iran. https://doi.org/10.24200/sci.2019.50212.1578
21. Song Y, Shan D, Chen R, Han E-H (2010) Effect of second phases on the corrosion behavior of wrought Mg–Zn–Y–Zr alloy. Corros Sci 52:1830–1837
22. Zong Y, Yuan G, Zhang X, Mao L, Niu J, Ding W (2012) Comparison of biodegradable behaviors of AZ31 and Mg–Nd–Zn–Zr alloys in Hank's physiological solution. Mater Sci Eng B 177:395–401
23. Liu H, Chen Y, Tang Y, Wei S, Niu G (2007) The microstructure, tensile properties, and creep behavior of as-cast Mg–(1–10)%Sn alloys. J Alloy Compd 440:122–126
24. Nayyeri G, Mahmudi R (2010) Enhanced creep properties of a cast Mg–5Sn alloy subjected to aging-treatment. Mater Sci Eng A 527:4613–4618
25. Wahba M, Katayama S (2012) Laser welding of AZ31B magnesium alloy to Zn-coated steel. Mater Design 35:701–706
26. Song GL, Atrens A (2003) Understanding magnesium corrosion, a framework for improved alloy performance. Adv Eng Mater 5:837–858
27. American Society for Testing and Materials (2004) ASTM-G31-72: standard practice for laboratory immersion corrosion testing of metals. In: Annual Book of ASTM Standards. Philadelphia, PA
28. Zhang E, Yang L (2008) Microstructure, mechanical properties and bio-corrosion properties of Mg–Zn–Mn–Ca alloy for biomedical application. Mater Sci Eng A 497:111–118
29. Zhang EL, Yang L, Xu JW, Chen HY (2010) Mechanical properties and bio-corrosion properties of Mg–Si(–Ca, Zn) alloy for biomedical application. Acta Biomater 6:1756–1762
30. Shi ZM, Atrens A (2011) An innovative specimen configuration for the study of Mg corrosion. Corros Sci 53:226–246
31. Xin RL, Li B, Liu Q (2011) Influence of texture on corrosion rate of AZ31 Mg alloy in 3.5 wt% NaCl. Mater Design 32:4548–4552
32. Turan ME, Sun Y, Akgul Y, Turen Y, Ahlatci H (2017) The effect of GNPs on wear and corrosion behaviors of pure magnesium. J Alloy Compd 724:14–23
33. Khalilpour H, Miresmaeili SM, Baghani A (2016) The microstructure and impression creep behavior of cast Mg–4Sn–4Ca alloy. Mater Sci Eng A 652:365–369
34. Ha HY, Kang JY, Yim CD, Yang J, You BS (2014) Role of hydrogen evolution rate in determining the corrosion rate of extruded Mg–5Sn–(1–4wt%) Zn alloys. Corros Sci 89:275–285
35. Zhang B, Hou Y, Wang X, Wang Y, Geng L (2011) Mechanical properties, degradation performance and cytotoxicity of Mg–Zn–Ca biomedical alloys with different compositions. Mater Sci Eng C 31:1667–1673
36. Cheng W-L, Wang M, Que Z-P, Xu C-X, Zhang J-S, Liang W, You B-S, Park S-S (2013) Microstructure and mechanical properties of high speed indirect-extruded Mg–5Sn–(1,2,4) Zn alloys. J Cent South Univ 20:2643–2649
37. Kuwahara H, Al-Abdullat Y, Mazaki N, Tsutsumi S, Aizawa T (2001) Precipitation of magnesium apatite on pure magnesium surface during immersing in Hank's solution. Mater Trans 42:1317–1321
38. Zhang S, Li J, Song Y, Zhao C, Zhang X, Xie C, Zhang Y, Tao H, He Y, Jiang Y, Bian Y (2009) In vitro degradation, hemolysis and MC3T3-E1 cell adhesion of biodegradable Mg–Zn alloy. Mater Sci Eng C 29:1907–1912
39. ASM Handbook (1961) USA
40. Czerwinski F (2008) Magnesium injection molding. Springer, New York
41. Zeng RC, Zhang J, Huang WJ, Dietzel W, Kainer KU, Blawert C, Ke W (2006) Review of studies on corrosion of magnesium alloys. Trans Nonferr Met Soc China 16:763–771
42. Gray-Munro JE, Seguin C, Strong M (2009) Influence of surface modification on the in vitro corrosion rate of magnesium alloy AZ31. J Biomed Mater Res A 91A:221–230
43. Li Z, Gu X, Lou S, Zheng Y (2008) The development of binary Mg–Ca alloys for use as biodegradable materials within bone. Biomaterials 29:1329–1344
44. Wang Y, Wei M, Gao J, Hu J, Zhang Y (2008) Corrosion process of pure magnesium in simulated body fluid. Mater Lett 62:2181–2184
45. Wang HX, Guan SK, Wang X, Ren CX, Wang LG (2010) In vitro degradation and mechanical integrity of Mg–Zn–Ca alloy coated with Ca-deficient hydroxyapatite by the pulse electrodeposition process. Acta Biomater 6:1743–1748
46. Song GL (2007) Control of biodegradation of biocompatible magnesium alloys. Corros Sci 49:1696–1701
47. Yim CD, Woo SK, You BS (2015) Effect of Sn: Zn ratio on corrosion behaviour of Mg–aSn–bZn extrusions. In: Manuel MV, Singh A, Alderman M, Neelameggham NR (eds) Magnesium technology. Springer, Berlin, pp 315–318
48. Gu X-N, Zheng Y-F, Cheng Y, Zhong S-P, Xi T-F (2009) In vitro corrosion and biocompatibility of binary magnesium alloys. Biomaterials 30:484–498

Publisher's Note Springer Nature remains neutral with regard to jurisdictional claims in published maps and institutional affiliations.